Journal of Power Sources 187 (2009) 123–135

Contents lists available at ScienceDirect

Journal of Power Sources

journal homepage: www.elsevier.com/locate/jpowsour

Multidimensional flow, thermal, and chemical behavior in solid-oxide fuel cell button cells

Graham M. Goldin[a,*], Huayang Zhu[b], Robert J. Kee[b], David Bierschenk[c], Scott A. Barnett[c]

[a] Ansys Incorporated, 10 Cavendish Ct., Centerra Resource Park, Lebanon, NH 03766, USA
[b] Engineering Division, Colorado School of Mines, Golden, CO 80401, USA
[c] Materials Science, Northwestern University, Evanston, IL 60208, USA

ARTICLE INFO

Article history:
Received 19 September 2008
Received in revised form 21 October 2008
Accepted 22 October 2008
Available online 5 November 2008

Keywords:
SOFC
Button cell
Modeling
Computational fluid dynamics

ABSTRACT

The quantitative analysis and interpretation of button-cell experiments usually depends upon assuming isothermal conditions together with uniform and known gas composition within the gas compartments. An objective of the present effort is to develop computational tools to study the validity of such assumptions. A three-dimensional computational fluid dynamics (CFD) model is developed and applied to a particular SOFC button cell, characterizing the fluid flow, chemistry, and thermal transport. Results show that when inlet flow rates are sufficiently high, button-cell data can be interpreted using the commonly used assumptions. However, when flow rates are not sufficient, the assumptions of uniform composition can be significantly violated. Additionally, depending on operating conditions there can be significant temperature variations within the gas compartments and the membrane–electrode assembly.

1. Introduction

The primary objective of this paper is to use a three-dimensional computational model to explore the performance of a particular solid-oxide fuel cell (SOFC) button cell over a range of operating conditions. A supporting objective is to report on the development of a three-dimensional computational fluid dynamics (CFD) model that extends the state of the art, especially in its ability to represent elementary chemistry and electrochemistry. Although the study considers a particular cell geometry, significant broader implications can be inferred from the results.

Button cells play a major role in the development and evaluation of new SOFC materials and membrane–electrode assembly (MEA) architectures. The underpinning models that describe material combinations and MEA architectures are usually developed and validated with small button-cell experiments. Quantitative predictive simulations are playing increasingly important roles in the development of fuel-cell stacks and systems. Thus, it is important that laboratory-scale experimental observations can be interpreted quantitatively and unambiguously. Understanding the influence of experimental configurations and operating conditions on measured cell performance is essential to the development and validation of predictive models at the system level.

Although there are many variants of button-cell experiments, most share some common characteristics. The button cell illustrated in Fig. 1, which represents an experiment developed by Barnett and co-workers [1], is typical and serves as the focus of the modeling in this paper. The cylindrical MEA is bonded to a ceramic support tube and the entire assembly positioned within a temperature-controlled furnace. Fuel is supplied via a tube onto the anode side of the MEA. The cathode side is exposed to air, which may simply be the furnace air or may be supplied via a feed tube. The assembly shown in Fig. 1 is oriented horizontally. Others position the assembly vertically. Button-cell experiments should usually be designed and operated such that the gas-phase composition at MEA interfaces is known and is spatially uniform across the surface of the MEA. As a result, any complications associated with gas-phase fluid flow can be removed from interpreting the electrochemical performance. Depending upon gas flow rates, the gas-phase composition at the electrode faces can be significantly different from the composition entering through the feed tubes.

Commercial CFD software can be used directly, or modified, to model aspects of fuel-cell operation, especially considering flow in complex geometries. Indeed, there is significant and beneficial use of such models to assist the design and development of cells and stacks. However, current software and models are usually limited in their ability to model details of transport, chemistry, and electrochemistry. For example, internal reforming chemistry is handled almost exclusively with two global reactions (steam reforming and water-gas shift) that use highly empirical rate expressions. Charge-transfer chemistry usually relies upon a global Butler–Volmer

* Corresponding author. Tel: +1 603 727 5578; fax: +1 603 643 3967.
E-mail address: graham.goldin@ansys.com (G.M. Goldin).

0378-7753/$ – see front matter © 2008 Elsevier B.V. All rights reserved.
doi:10.1016/j.jpowsour.2008.10.097

Nomenclature

A_{des}	pre-exponential factor for H_2desorption ($m^2\,s\,mol^{-1}$)
A_s	specific surface area of the active catalysts (m^{-1})
B_g	permeability (m^2)
D_k^e	effective diffusion coefficients ($m^2\,s^{-1}$)
$\mathcal{D}_{kj}$	binary diffusion coefficients ($m^2\,s^{-1}$)
D_k^{Kn}	effective Knudsen diffusion coefficients ($m^2\,s^{-1}$)
E_{cell}	cell potential (V)
E_{des}	activation energy for H_2 desorption ($J\,mol^{-1}$)
E_{el}	activation energy of electric conductivity of the electrolyte ($J\,mol^{-1}$)
E_{H_2}	activation energy for H_2 electrochemical oxidation ($J\,mol^{-1}$)
E_{O_2}	activation energy for O_2 electrochemical reduction ($J\,mol^{-1}$)
E_{rev}	reversible cell potential (V)
F	Faraday constant ($C\,mol^{-1}$)
Gr	Grashof number
$\mathbf{g}$	acceleration of the gravity ($m\,s^{-2}$)
h	enthalpy of the gas-phase mixture ($J\,kg^{-1}$)
h_k	enthalpy of the k th species ($J\,kg^{-1}$)
i	net current density ($A\,m^{-2}$)
i_0	exchange current density ($A\,m^{-2}$)
i_0^a	exchange current density for H_2 oxidation ($A\,m^{-2}$)
i_0^c	exchange current density for O_2 reduction ($A\,m^{-2}$)
$i^*_{H_2}$	parameter in the expression of i_0^a ($A\,m^{-2}$)
$i^*_{O_2}$	parameter in the expression of i_0^c ($A\,m^{-2}$)
$\mathbf{J}_k$	gas-phase species mole flux ($mol\,m^{-2}\,s^{-1}$)
$\mathbf{j}_k$	gas-phase species mass flux ($kg\,m^{-2}\,s^{-1}$)
$\mathbf{J}_k^a$	gas-phase species mole flux within the anode ($mol\,m^{-2}\,s^{-1}$)
$\mathbf{J}_k^c$	gas-phase species mole flux within the cathode ($mol\,m^{-2}\,s^{-1}$)
$J^{el}_{H_2,a}$	molar flux of H_2 ($mol\,m^{-2}\,s^{-1}$)
$J^{el}_{H_2O,a}$	molar flux of H_2O ($mol\,m^{-2}\,s^{-1}$)
$J^{el}_{O_2,c}$	molar flux of O_2 ($mol\,m^{-2}\,s^{-1}$)
K_g	number of gas-phase species
K_s	number of surface-adsorbed species
L	characteristic length (m)
L_{el}	electrolyte thickness (m)
p	pressure (Pa)
$p_{H_2,a}$	partial pressure of H_2 (Pa)
$p_{H_2O,a}$	partial pressure of H_2O (Pa)
$p_{O_2,c}$	partial pressure of O_2 (Pa)
$p^*_{H_2}$	parameter in the expression of i_0^a (Pa)
$p^*_{O_2}$	parameter in the expression of i_0^c (Pa)
q''_{rad}	radiative heat flux ($J\,m^{-2}\,s^{-1}$)
R	universal gas constant ($J\,mol^{-1}\,K^{-1}$)
Re	Reynolds number
r_p	pore radius (m)
$\dot{s}_k$	molar production rate by surface reactions ($mol\,m^{-2}\,s^{-1}$)
T	temperature (K)
T_{surf}	MEA surface temperature (K)
T_{ref}	reference temperature (K)
T_∞	furnace temperature (K)
U	characteristic velocity ($m\,s^{-1}$)
$\mathbf{V}$	gas-phase velocity ($m\,s^{-1}$)
W_{H_2}	molecular weight of H_2 ($kg\,mol^{-1}$)
W_k	species molecular weight ($kg\,mol^{-1}$)
$\overline{W}$	mean molecular weight ($kg\,mol^{-1}$)
X_k	gas-phase species mole fractions
Y_k	gas-phase species mass fractions

Greek letters

$\alpha_{a,a}$	anodic symmetric factor in the BV equation at the anode
$\alpha_{c,a}$	cathodic symmetric factor in the BV equation at the anode
$\alpha_{a,c}$	anodic symmetric factor in the BV equation at the cathode
$\alpha_{c,c}$	cathodic symmetric factor in the BV equation at the cathode
β	volumetric thermal expansion coefficient
Γ	surface site density ($mol\,m^{-2}$)
γ_0	stick coefficient of H_2 adsorption
ε	MEA surface emissivity
η_{ohm}	ohmic overpotential (V)
$\eta_{act,a}$	activation overpotential at the anode (V)
$\eta_{act,c}$	activation overpotential at the cathode (V)
θ_k	site fractions of surface-adsorbed species
λ	heat conductivity ($J\,m^{-1}\,K\,s$)
λ^{eff}	effective heat conductivity ($J\,m^{-1}\,K^{-1}\,s^{-1}$)
λ^g	gas-phase heat conductivity ($J\,m^{-1}\,K^{-1}\,s^{-1}$)
λ^s	solid-phase heat conductivity ($J\,m^{-1}\,K^{-1}\,s^{-1}$)
μ	gas-phase viscosity ($kg\,cm^{-1}\,s^{-1}$)
μ_k	species chemical potentials ($J\,mol^{-1}$)
μ_{H_2O}	chemical potentials of H_2O ($J\,mol^{-1}$)
μ_{H_2}	chemical potentials of H_2 ($J\,mol^{-1}$)
μ_{O_2}	chemical potentials of O_2 ($J\,mol^{-1}$)
μ_k°	species standard-state chemical potentials ($J\,mol^{-1}$)
$\mu^\circ_{H_2}$	standard-state chemical potential of H_2 ($J\,mol^{-1}$)
$\mu^\circ_{H_2O}$	standard-state chemical potential of H_2O ($J\,mol^{-1}$)
$\mu^\circ_{O_2}$	standard-state chemical potential of O_2 ($J\,mol^{-1}$)
ρ	gas-phase mass density ($kg\,m^{-3}$)
σ	Stefan–Boltzmann constant ($W\,m^{-2}\,K^{-4}$)
τ	tortuosity
ϕ	porosity

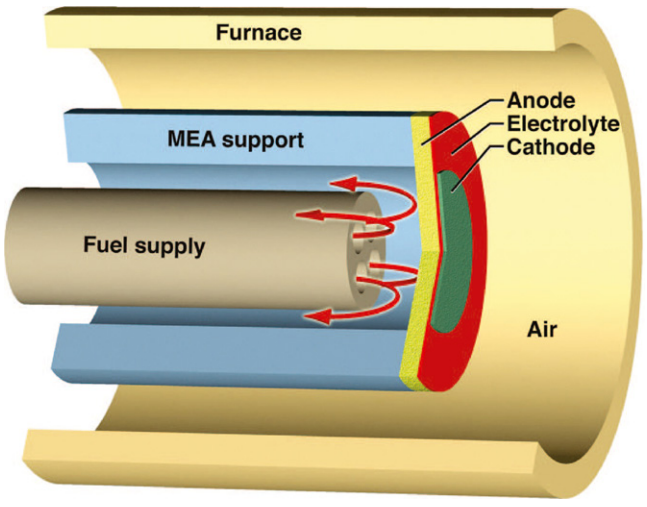

Fig. 1. Illustration of a nominal button-cell system.

formulation. Porous-media transport is handled in terms of Darcy flow. The model reported herein relaxes all of these assumptions, and thus contributes to the continuing development of high level CFD software.

Several two- and three-dimensional models have been published [2–7] that specifically consider button-cell performance. Janardhanan and Deutschmann [3] and Shi et al. [5,6] modeled axisymmetric (two-dimensional) button cells, but assumed isothermal conditions. The present three-dimensional, non-isothermal, model significantly extends these earlier contributions.

2. Mathematical models

The model provides the capability for full three-dimensional fluid flow, heat and mass transport, porous-media transport and chemistry throughout the gas compartments and the MEA. In the open gas compartments (i.e., outside the porous electrodes) the flow is represented by the Navier–Stokes equations. The chemistry and porous-media models are based upon models developed by Zhu et al. [8,9]. The solutions are constrained by boundary conditions as well as interface conditions between porous electrodes and the gas compartments.

2.1. Gas-phase transport

Within the gas compartments, the steady-state mass-, species-, momentum-, and energy-conservation equations are stated generally in vector form as

$$\nabla \cdot (\rho \mathbf{V}) = 0, \tag{1}$$

$$\nabla \cdot (\rho Y_k \mathbf{V}) = -\nabla \cdot \mathbf{j}_k, \tag{2}$$

$$\nabla \cdot (\rho \mathbf{V}\mathbf{V}) = \nabla \cdot \left[\mu(\nabla \mathbf{V} + (\nabla \mathbf{V})^{\mathrm{T}}) - \frac{2}{3}\mu(\nabla \cdot \mathbf{V})\mathrm{I}\right] - \nabla p + \rho \mathbf{g} \tag{3}$$

$$\nabla \cdot (\rho h \mathbf{V}) = \nabla \cdot \left(\lambda \nabla T - \sum_{k=1}^{K_\mathrm{g}} h_k \mathbf{j}_k\right), \tag{4}$$

$$\rho = \frac{p_\mathrm{o}}{RT \sum_{k=1}^{K_\mathrm{g}} Y_k / W_k}. \tag{5}$$

In these equations the independent variables are the spatial coordinates. The dependent variables are the mass density ρ, velocity $\mathbf{V}$, pressure p, mass fractions Y_k, and temperature T. The nominally uniform pressure used in the equation of state is p_o. The species diffusive mass flux is represented as $\mathbf{j}_k$, which is evaluated according to ordinary multicomponent diffusion. Thermodynamic properties include the mixture specific enthalpy h, and species specific enthalpies h_k, all of which are known functions of temperature. Transport properties include the gas-phase dynamic viscosity μ and the thermal conductivity λ. Other variables are the species molecular weights W_k and the acceleration of gravity $\mathbf{g}$.

2.2. Porous-media transport

Within the porous electrodes, the steady-state mass-, species-, momentum-, and energy-conservation equations are stated in vector form as

$$\nabla \cdot (\rho \mathbf{V}) = 0, \tag{6}$$

$$\nabla \cdot (\rho Y_k \mathbf{V}) = -\nabla \cdot \mathbf{j}_k + \dot{s}_k A_\mathrm{s} W_k, \quad (k = 1, \ldots, K_\mathrm{g}) \tag{7}$$

$$\nabla \cdot (\rho \mathbf{V}\mathbf{V}) = -\nabla p + \rho \mathbf{g} - \frac{\mu}{B_\mathrm{g}} \mathbf{V}, \tag{8}$$

$$\nabla \cdot (\rho h \mathbf{V}) = \nabla \cdot \left(\lambda^{\mathrm{eff}} \nabla T - \sum_{k=1}^{K_\mathrm{g}} h_k \mathbf{j}_k\right) + \sum_{k=1}^{K_\mathrm{g}} \dot{s}_k A_\mathrm{s} W_k h_k, \tag{9}$$

$$\dot{s}_k(\theta_k) = 0, \quad (k = 1, \ldots, K_\mathrm{s}) \tag{10}$$

In these equations the independent variables are the spatial coordinates. The dependent variables are the mass density ρ, velocity $\mathbf{V}$, pressure p, mass fractions Y_k of the K_g gas-phase species, and coverages θ_k of the K_s surface-adsorbed species. Viscous drag within the porous electrodes is represented as a Darcy loss, where B_g is the permeability.

Within the porous media, the gas and solid phases are assumed to have the same temperature T. The effective thermal conductivity λ^{eff} considers both gas- and solid-phase contributions as

$$\lambda^{\mathrm{eff}} = \phi \lambda^{\mathrm{g}} + (1 - \phi)\lambda^{\mathrm{s}}, \tag{11}$$

where ϕ is the porosity and λ^{s} is the solid-phase thermal conductivity. For Ni-YSZ, $\lambda^{\mathrm{s}} \approx 11\ \mathrm{W\ m^{-1}\ K^{-1}}$.

Heterogeneous reactions can occur on the solid surfaces within the porous anode structure. The molar production rates of gas-phase species via heterogeneous surface reaction are represented as $\dot{s}_k$ (Eqs. (7) and (9)). The effective catalytic specific surface area ($\mathrm{m^2\ m^{-3}}$) is represented as A_s. Eq. (10) represents the fact that the net production rates of the K_s surface-adsorbed species must vanish at steady state. The production rates of surface species depend upon temperature, pressure, gas-phase composition, and the coverages of surface species θ_k. Details about formulation of the heterogeneous chemistry may be found in Kee et al. [10].

2.3. Interface conditions

The model does not consider spatial variations within the thin dense electrolyte and the cathode. Moreover, the anode charge transfer is confined to a thin layer at the interface between the dense electrolyte and the porous anode structure. In other words, all the electrochemistry and ion transport is confined to an infinitely thin layer, and thus the behavior is represented in terms of interface conditions. This approximation is based upon the results of previously published models that spatially resolve the thin charge-transfer region, showing that charge transfer is accomplished within a few tens of microns [9,11].

Consider first the interface between the fuel compartment and the porous anode. The solutions to Eqs. (1)–(9) are constrained to require that the fluxes of mass, species, momentum, and energy are continuous across the interface. Additionally, radiation heat transfer from the face of the porous electrode is found to have a significant impact on the MEA temperature.

Anodic charge-transfer chemistry proceeds at the interface between the dense electrolyte and the porous anode structure. The result is a net molar flux of gas-phase species into and out of the anode pore spaces as represented as $\mathbf{J}_k^{\mathrm{a}}$. Cathodic charge-transfer chemistry proceeds at the interface between the thin cathode and the air compartment. In this case, the net flux of oxygen between the air and the cathode is represented as $\mathbf{J}_k^{\mathrm{c}}$.

In addition to the species fluxes, the model must also represent other important processes within the thin membrane–electrode assembly. Irreversible polarization losses associated with the electrochemical charge-transfer chemistry manifest themselves as heat. The heating rate is evaluated from the enthalpy fluxes to and from the thin MEA layer. The electrical power density produced by the cell is represented as iE_{cell}, where i is the electrical current density and E_{cell} is the cell operating potential. This electrical energy is subtracted from the thermal energy balance. There is also a thermal-radiation loss from the cathode side of the MEA.

2.4. Boundary conditions

Boundary conditions for the gas flows are relatively straightforward. The composition, velocity, and temperature of the fuel inlet is specified. The fuel-side outflow boundary is specified by specifying the exit pressure. The particular reactor used in this study uses an unforced air supply on the cathode side. Thus the boundary condition is specified as the composition of air at atmospheric pressure and at furnace temperature.

There are several solid surfaces in the model, not including the porous media. These include the fuel feed tube and the cylindrical structure that supports the button cell. All these solid surfaces are taken to be isothermal at a specified furnace temperature and the velocity vanishes on all the solid surfaces. Additionally, the solid surfaces are assumed to be chemically inert, such that the species fluxes normal to the surface vanish.

2.5. Thermal radiation

Despite the fact that temperatures and temperature differences are relatively low, there is the possibility of thermal radiation from the surfaces of the MEA. Although the thermal radiation is weak, the low flow rates also cause a weak convective interaction between the gas compartments and the MEA. The present study uses a relatively simple radiation model in which the surfaces of the MEA radiate to a black-body enclosure at the nominal furnace temperature. That is, the radiative flux from the MEA surfaces is evaluated as

$$q''_{\mathrm{rad}} = \epsilon\sigma(T^4_{\mathrm{surf}} - T^4_{\infty}), \tag{12}$$

where σ is the Stefan–Boltzmann constant, T_{surf} is the MEA surface temperature, and T_{∞} is the furnace temperature. In the present study, the emissivity of the MEA surfaces is taken to be $\epsilon = 0.8$. This value is larger than the emissivities of smooth Nickel or Ziconia since the anode pore spaces trap incident radiation.

2.6. Diffusion model

The diffusion mass-flux vector, $\mathbf{j}_k$, is modeled in both gas-phase fuel and air chambers, as well as the porous anode, using a Fickian model:

$$\mathbf{j}_k = -\rho D^{\mathrm{e}}_k \nabla Y_k. \tag{13}$$

For the fuel and air chambers, the effective diffusion coefficient D^{e}_k is the mean bulk diffusion coefficient, D^{m}_k, calculated as,

$$D^{\mathrm{m}}_k = \frac{1 - X_k}{\sum_{k \neq j} X_j / (\gamma \mathcal{D}_{kj})}, \tag{14}$$

where X_k are the mole fractions, $\mathcal{D}_{kj}$ are the binary diffusion coefficients determined from kinetic theory [10], and $\gamma = 1$.

Within the porous anode, the effective mixture-averaged diffusion coefficients are evaluated using the Bosanquet formula,

$$\frac{1}{D^{\mathrm{e}}_k} = \frac{1}{D^{\mathrm{m}}_k} + \frac{1}{D^{\mathrm{Kn}}_k}. \tag{15}$$

The mean bulk diffusion coefficients D^{m}_k are evaluated from Eq. (14) with γ set to ϕ/τ, where ϕ is the porosity and τ is the tortuosity.

The Knudsen diffusion coefficient in Eq. (15) is calculated as

$$D^{\mathrm{Kn}}_k = \frac{2}{3}\frac{\phi}{\tau} r_{\mathrm{p}} \sqrt{\frac{8RT}{\pi W_k}}, \tag{16}$$

where r_{p} is the mean pore radius.

The results reported in this paper assume that the anode porous matrix is homogenous and isotropic. However the model itself is capable of spatially varying and anisotropic properties, which may be needed to represent certain functionally graded electrode structures.

2.7. Heterogeneous chemistry

Heterogeneous chemistry (e.g., reforming, partial oxidation, etc.) occurs on active catalyst surfaces within the porous anode structure. Although the models and software are quite general and accept alternative reaction mechanisms, the mechanism used in the present study considers reaction within Ni-YSZ cermet structures. This reaction mechanism, which has been validated and documented previously [3,8], consists of 42 reactions among 6 gas-phase species and 12 surface-adsorbed species.[1] The surface reaction rates have Arrhenius temperature dependence, and some reactions have activation energies that are functions of the surface coverages.

This catalytic reaction mechanism spans the conditions between steam reforming, autothermal reforming, dry reforming (i.e., reforming of CH_4 by CO_2), and catalytic partial oxidation. This approach is quite different from, and more capable than, most published SOFC models, which usually incorporate two global reactions for steam reforming and water gas shift. The global approach requires empirical rate expression for the global reactions. The present elementary mechanism does not directly include a steam-reforming or a water-gas-shift reaction. Rather, the processes are represented by combinations of elementary reactions. This fundamental approach enables predictive capabilities over wide operating conditions, spanning steam reforming, autothermal reforming, and partial oxidation. Water-gas-shift chemistry is also fully represented within the reaction mechanism.

2.8. Electrochemistry

The operating cell potential E_{cell} can be written in terms of overpotentials as

$$E_{\mathrm{cell}} = E_{\mathrm{rev}} - \eta_{\mathrm{act},a}(i) - |\eta_{\mathrm{act},c}(i)| - \eta_{\mathrm{ohm}}(i). \tag{17}$$

In Eq. (17), E_{rev} is the reversible (Nernst) potential across the dense electrolyte, η_{ohm} is the ohmic overpotential, and $\eta_{\mathrm{act,a}}$ and $\eta_{\mathrm{act,c}}$ are the activation overpotentials at the anode–electrolyte and cathode–electrolyte interfaces, respectively. All the overpotentials depend upon the current density. Because species transport and chemistry are fully resolved within the anode, a model for concentration overpotential is not needed.

In a typical porous, cermet, composite, electrode, electrochemical reactions occur within a very thin region (tens of microns) adjacent to the dense electrolyte [9,11]. With a button cell that is on the order of 1 mm thick, it is not necessary to resolve the charge-transfer region spatially. Rather, it is sufficient to approximate the charge-transfer behavior as though it proceeds at a surface. In this approach, geometric factors such as the three-phase-boundary lengths are subsumed into expression for the exchange current densities [8].

The results in this paper are based upon assuming that electro-oxidation of the fuel proceeds entirely via H_2. It is known that CO, and possibly hydrocarbons, can participate in charge-transfer reactions [12,13]. However, the charge-transfer rates are greatly higher for H_2. Moreover, catalytic water-gas-shift processes (globally,

[1] The mechanism is available for download at http://www.detchem.com.

$CO + H_2O \leftrightharpoons CO_2 + H_2$) readily convert CO to H_2. Consequently it is a reasonable to use the widely used approximation that charge transfer proceeds through H_2. As ongoing research reveals the information needed to establish the fundamental reaction pathways and rates for parallel charge-transfer processes, they can be incorporated into models such as the ones discussed here. However, assuming H_2 charge transfer is entirely sufficient for the purposes of the present paper, which focuses upon thermal and flow behaviors.

Assuming that electro-oxidation of the fuel proceeds dominantly via H_2, the reversible potential can be calculated from the Nernst equation as

$$E_{\text{rev}} = \frac{1}{2F}\left(\mu^{\circ}_{H_2} + \frac{1}{2}\mu^{\circ}_{O_2} - \mu^{\circ}_{H_2O}\right) + \frac{RT}{2F}\ln\left(\frac{p_{H_2,a}p^{1/2}_{O_2,c}}{p_{H_2O,a}}\right), \quad (18)$$

where F is the Faraday constant, μ°_k are standard-state chemical potentials, p_k are species partial pressures (measured in atmospheres). Subscripts a and c denote anode-side and cathode-side, respectively. Any small losses due to electrical current leakage through the dense electrolyte are neglected.

Zhu et al. [8] derived and validated a modified Butler–Volmer formulation, which is based upon a multi-step H_2 electrochemical oxidation process with a single rate-limiting step. At the anode–electrolyte interface, the current density is represented as

$$\frac{i}{i^{a}_0} = \exp\left(\frac{\alpha_{a,a}F\eta_{\text{act},a}}{RT}\right) - \exp\left(\frac{-\alpha_{c,a}F\eta_{\text{act},a}}{RT}\right), \quad (19)$$

where i^{a}_0 is the anode exchange current density, and $\alpha_{a,a}$ and $\alpha_{c,a}$ are the anodic and cathodic symmetry parameters, respectively. The anode exchange current density is calculated as

$$i^{a}_0 = i^{*}_{H_2}\exp\left[-\frac{E_{H_2}}{R}\left(\frac{1}{T} - \frac{1}{T_{\text{ref}}}\right)\right]\frac{(p_{H_2}/p^{*}_{H_2})^{\alpha_{a,a}/2}(p_{H_2O})^{1-\alpha_{a,a}/2}}{1 + (p_{H_2}/p^{*}_{H_2})^{1/2}}, \quad (20)$$

where E_{H_2} is the apparent activation energy and $i^{*}_{H_2}$ is an empirical constant that is adjusted to fit experiments at a reference temperature T_{ref}. The term $p^{*}_{H_2}$ is derived for a steady hydrogen adsorption–desorption balance:

$$p^{*}_{H_2} = \frac{A_{\text{des}}\Gamma^2\sqrt{2\pi RTW_{H_2}}}{\gamma_o}\exp\left(-\frac{E_{\text{des}}}{RT}\right), \quad (21)$$

where the pre-exponential factor A_{des}, the activation energy E_{des}, the surface site density Γ, and the sticking coefficient γ_o are constants and W_{H_2} is the molecular weight of atomic hydrogen.

At the cathode–electrolyte interface, the modified Butler–Volmer equation is

$$\frac{i}{i^{c}_0} = \exp\left(\frac{\alpha_{a,c}F\eta_{\text{act},c}}{RT}\right) - \exp\left(\frac{-\alpha_{c,c}F\eta_{\text{act},c}}{RT}\right). \quad (22)$$

The cathode exchange current density is evaluated using

$$i^{c}_0 = i^{*}_{O_2}\exp\left[-\frac{E_{O_2}}{R}\left(\frac{1}{T} - \frac{1}{T_{\text{ref}}}\right)\right]\frac{(p_{O_2}/p^{*}_{O_2})^{\alpha_{a,c}/2}}{1 + (p_{O_2}/p^{*}_{O_2})^{1/2}}, \quad (23)$$

where E_{O_2} is the apparent activation energy for the electrochemical reduction of O_2, $i^{*}_{O_2}$ is an adjustable constant, and $p^{*}_{O_2}$ is written in Arrhenius form. Further details are found in Zhu et al. [8].

The ohmic overpotential (Eq. (17)) is modeled in terms of O^{2-} ion transport resistance within the dense YSZ electrolyte,

$$\eta_{\text{ohm}} = \frac{iL_{\text{el}}}{\sigma_0 T^{-1}\exp(-E_{\text{el}}/RT)}. \quad (24)$$

In this expression L_{el} is the electrolyte thickness and the denominator is the temperature-dependent ion conductivity.

The current density i is determined by substituting Eqs. (18)–(24) into Eq. (17). The species molar fluxes due to electrochemistry, J^{el}_k are determined from the current density as $J^{\text{el}}_{H_2,a} = -i/2F$, $J^{\text{el}}_{H_2O,a} = i/2F$ and $J^{\text{el}}_{O_2,c} = -i/4F$.

3. Numerical method

The conservation equations are discretized using an unstructured finite-volume method with second-order reconstruction of the convective and diffusive fluxes for all equations [14]. This approach enables the incorporation of three-dimensional geometric complexity, using geometry-definition and automated mesh-discretization software (e.g., GAMBIT).

At all materials interfaces, there are finite-volume cells that abut the interface. In a finite-volume setting, the conservation equations are represented in an integral sense for each finite volume. Away from material interfaces, fluxes leaving one cell must be identical to the fluxes entering the neighboring cell. At material interfaces, however, certain physical or chemical behaviors can manifest themselves as sources of mass, energy, etc. For example, thermal radiation at the interface between a porous material and the neighboring gas flow represents a loss (or gain) in thermal energy for the finite volumes that span the interface. A thin (i.e., not spatially resolved) MEA is a more complex interface. The charge-transfer chemistry causes gas-phase species fluxes into and out of neighboring finite volumes. Moreover, there are important thermal consequences. Polarization losses associated with charge-transfer chemistry and Joule heating associated with ion current through the dense electrolyte are sources of thermal energy at the interface. However, net electrical power delivered to an external load (i.e., iE_{cell}) does not contribute to the thermal balance.

The system of equations is solved using a segregated SIMPLEalgorithm, in which the mass-continuity equation (Eqs. (1) and (6)) are recast as a pressure-correction equations and solved together with the momentum equations (i.e., Eqs. (3) and (8)) [15]. The species-continuity and thermal-energy equations are similarly linearized. The inner linear problem is solved using an algebraic multigrid (AMG) method [16]. An outer iteration is used to solve the full nonlinear problem.

The software is written in C++ using object-oriented programming techniques, and interfaced with the scriptable PYTHONlanguage. The CANTERA[2] software, which is also written in C++, is used to evaluate thermodynamic quantities (enthalpies, heat capacities, Nernst potentials), transport properties (viscosities, thermal conductivities, species diffusivities) and reaction rates [17].

3.1. Verification

The software that implements the model is large and complex, providing three-dimensional geometrical generality and the incorporation of extensive chemical and physical processes. Thus, as in all major software development, comprehensive verification is an important aspect of effort. In this context, verification is concerned primarily with assuring that the software solves accurately the underlying physical model. Software verification, per se, is less concerned with validating the physical and chemical formulations, which usually rely upon experimental measurements and their interpretation. Of course, validating the underpinning physics and chemistry is also an important objective.

[2] See http://www.cantera.org.

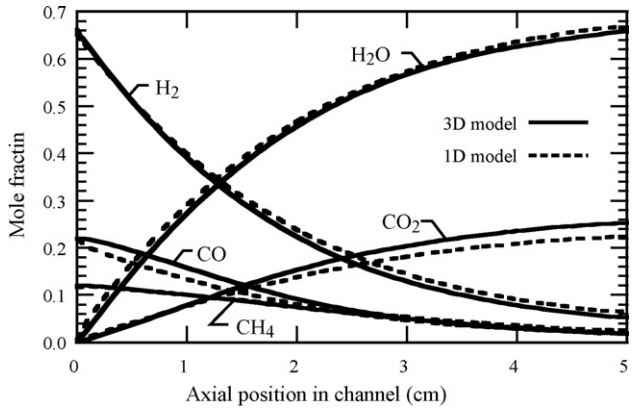

Fig. 2. Gas-phase mole fractions along the centerline of an SOFC planar fuel channel. Predictions from the current CFD model are shown as solid lines and predictions from a plug-flow model [8] are shown as dashed lines.

The object-oriented program structure enables the independent testing and validation of all the sub-models (thermodynamic and transport property evaluations, chemical kinetics, etc.). Additionally, the present model has been tested against other independently developed models that solve similar problems. Such model-to-model comparisons are an important aspect of model development and validation. For example, the three-dimensional model was tested by comparing a planar SOFC channel simulation with results published by Zhu et al. [8], using conceptually identical, but independently programmed, submodels and model parameters.

Fig. 2 compares gas-phase mole fractions along the anode-channel centerline. The present CFD model fully resolves the channel fluid flow while the model by Zhu et al. [8] assumes plug flow. The CFD model enables two-dimensional species transport within the anode while Zhu et al. neglect axial diffusive transport. Despite these differences in the underlying models, the results agree well. These comparisons serve to validate the current CFD model (especially the chemistry and electrochemistry submodels) as well as the low-dimensional approximations in the model by Zhu et al. It should also be noted that chemistry aspects of the Zhu et al. model were developed and validated using experimental data.

4. Specific button cell

The button-cell geometry used in the present effort represents an experimental facility developed by Barnett et al. [1]. As illustrated in Fig. 1, the cell consists of an inlet fuel tube (6.5 mm outside diameter) with four cylindrical fuel channels (1.8 mm diameter). The fuel tube is positioned coaxially with an alumina tube (9.5 mm inside diameter) that supports the MEA. The end of the fuel tube is positioned 3 mm from the MEA. Anode exhaust gases flow out axially through the annular space between the fuel tube and the MEA support tube.

The cathode side of the MEA is exposed to air within the furnace. As illustrated in Fig. 1 there is no forced-air supply. The assembly is mounted horizontally in a furnace whose walls are maintained at uniform temperature. Thus, three-dimensional effects associated with natural convection are a potential concern.

The MEA is fabricated using a Ni-YSZ porous anode that has a thickness of 0.7 mm and a diameter of 15.2 mm. The dense electrolyte is 10 μm of YSZ, and the cathode is 40 μm of porous YSZ-LSM. The cathode is only 8 mm in diameter, so does not span the entire diameter of the anode disk. Thus, only the inner section of the MEA is electrochemically active.

The geometry is symmetric about a 90° sector. However, because the cell is mounted horizontally, a 180° sector is modeled to include natural convection. Fig. 3 shows some of the unstructured mesh faces. In total the mesh is comprised of 77,336 cells.

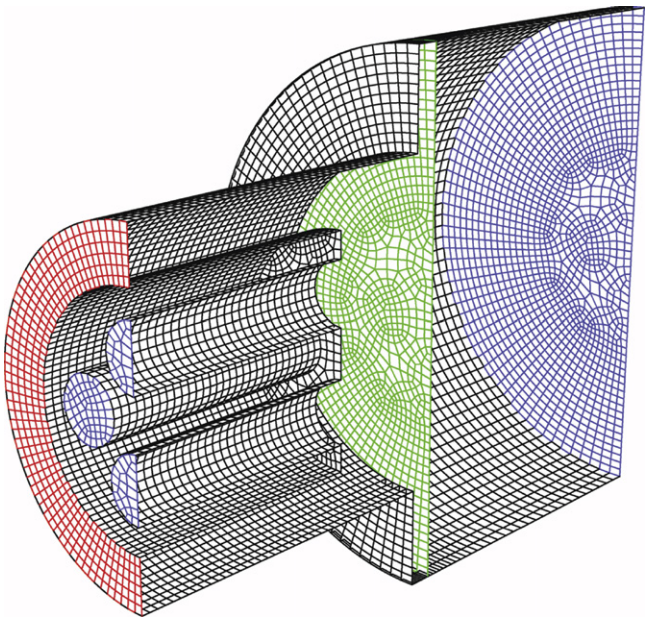

Fig. 3. Button-cell geometry and mesh, showing fuel-tube inlet and outlet, walls, MEA and air plenum.

The four-channel fuel tube is somewhat unusual; most button-cell experiments use a single inlet tube. While the present model uses the exact geometry for a particular experiment [1], the results depend only weakly on the inlet tube details. However, the results depend greatly upon inlet flow rates. It may be noted that the present study uses a relatively small button cell. Nevertheless, the general observations and insights from the study are applicable to larger cells.

5. Model parameters

Models such as the one here necessarily involve a number of parameters. Some, such as physical dimensions, are measured directly. However, as a practical matter, there are model parameters that must be established empirically. These usually involve electrochemical reaction rates and available three-phase boundary area, which are not measured independently. The parameters shown in Table 1 are determined to fit experimental data (Fig. 4) using humidified hydrogen fuel at nominal furnace temperatures of 700, 750 and 800 °C. The fuel flow rates are set to be sufficiently high that depletion and dilution are negligible (200 sccm). By flooding the cell, the charge-transfer parameters can be determined without concern for fluid-mechanical effects in the anode chamber. Once established, the parameters are held fixed for all other simulations in this study. Note that at 200 sccm, for the highest current density simulated (0.1V), the computed fuel depletion is 45%. In contrast, at the lowest flow rate simulated, 10 sccm, the fuel depletion is 73%.

Fig. 4 a compares measured and predicted polarization characteristics using the full three-dimensional model. It is evident that the set of model parameters produces an excellent representation of the data. Important fitted parameters include the exchange current factors $i^*_{H_2}$ and $i^*_{O_2}$, and the activation energies E_{H_2} and E_{O_2}. Although used as fitting parameters to match data in Fig. 4, all the parameters are physically reasonable. Nevertheless, it must be acknowledged that the set of parameters may not be entirely unique.

Table 1
Physical and chemical parameters for the MEA structure.

Parameters	Value	Units
Anode		
Thickness (L_a)	700	μm
Porosity (ϕ)	0.4	
Tortuosity (τ)	4.8	
Mean pore radius (r_p)	0.125	μm
Particle diameter (d_p)	1.0	μm
Specific catalyst area (A_s)	10000	cm^{-1}
Apparent activation energy (E_{H_2})	110.0	kJ mol^{-1}
Reference temperature (T_{ref})	1023.0	K
Exchange current factor ($i^*_{H_2}$)	1.25	A cm^{-2}
Anodic symmetry factor ($\alpha_{a,a}$)	1.5	
Cathodic symmetry factor ($\alpha_{c,a}$)	0.5	
$p^*_{H_2}$ pre-exponential (A_{des})	5.59E19	s cm^2 mol^{-1}
$p^*_{H_2}$ activation Energy (E_{des})	88.12	kJ mol^{-1}
$p^*_{H_2}$ surface site density (Γ)	2.6E-9	mol cm^{-2}
$p^*_{H_2}$ sticking probability (γ_o)	0.01	
Cathode		
Apparent activation energy (E_{O_2})	110.0	kJ mol^{-1}
Reference temperature (T_{ref})	1023.0	K
Exchange current factor ($i^*_{O_2}$)	1.25	A cm^{-2}
Anodic symmetry factor ($\alpha_{a,c}$)	0.875	
Cathodic symmetry factor ($\alpha_{c,c}$)	0.125	
Electrolyte: $\sigma_{el} = \sigma_0/T \exp(-E_{el}/RT)$		
Thickness (L_{el})	10	μm
Activation energy (E_{el})	80.11	kJ mol^{-1}
Ion conductivity pre-factor (σ_0)	1.786E5	s cm^{-1}

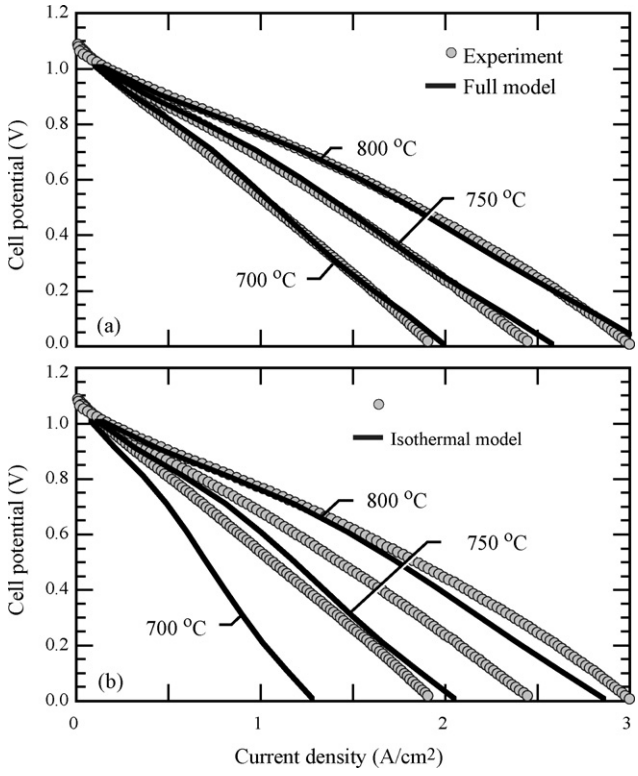

Fig. 4. Experimental and simulated polarization curves for a button cell operating with flooded (200 sccm) humidified H_2. The upper panel shows predictions with a full model that includes the energy equations and thus temperature distributions. Model parameters were established with the full model. The lower panel shows predicted polarization when assuming isothermal conditions at the nominal furnace temperature.

Button-cell data are generally reported at certain temperatures, usually inferring isothermal operation. However, as discussed subsequently, temperature can vary significantly throughout the MEA, especially at high current density. The MEA temperatures are usually greater than the furnace-wall temperature due to heat released by electrochemical reactions and Ohmic heating. Fig. 4 b shows predicted polarization behavior using the three-dimensional model, but without solving the energy equations and maintaining isothermal conditions of 700, 750 and 800 °C. By comparing predictions from the full model with those under isothermal conditions, it is evident that temperature variations within the MEA can have a significant effect on polarization behavior. These results show that assuming isothermal conditions when interpreting button-cell experiments can be misleading.

6. Performance on hydrogen

Fig. 5 shows experimentally measured characteristics for the button cell operating on humidified H_2, but at different fuel flow rates. At flow rates above 200 sccm, the fuel depletion is found to be negligible and the performance is essentially independent of flow rate. At low flow rates the effects of fuel depletion and dilution can be significant, especially at high current density. However, the polarization behavior is surprisingly weakly affected by the flow rate. Fig. 5 indicates the low flow rate (25 sccm) causes lower voltages, even at open circuit. However, the open-circuit potential should be independent of flow rate. The approximately 30 mV offset for the 25 sccm data is attributable to minor gas leaks in the experimental setup. The simulations neglect this leakage effect at all flow rates. With inlet fuel flow rates of 25 sccm, gas chromatography suggests that approximately 1% oxygen is getting into the fuel flow. This effect is too small to have any impact on cell performance at high flow rates.

Fig. 6 shows model predictions for low (25 sccm) and high (200 sccm) flow rates. In both cases the cell operating with a fuel mixture of 97% H_2, 3% H_2O. The wall temperatures and flow inlet temperatures are fixed at 800 °C. The operating potential is $E_{cell} = 0.5$ V. To help visualize the flow, path lines originating at the inlets are superimposed on the mole-fraction and temperature contours in Fig. 6. Because the flow field is essentially axisymmetric under these operating conditions, contours on half the symmetry plane are shown. Nevertheless, the simulations themselves are three-dimensional.

At low fuel flow rates, it is clear that the gas composition within the anode compartment varies significantly from the inlet composition. At sufficiently high flow rates, however, the composition at

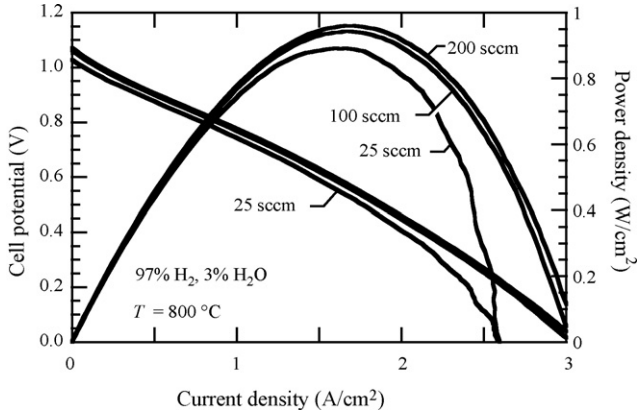

Fig. 5. Measured polarization behavior at different fuel flow rates. In all cases, the fuel is humidified H_2 and the nominal temperature is 800 °C.

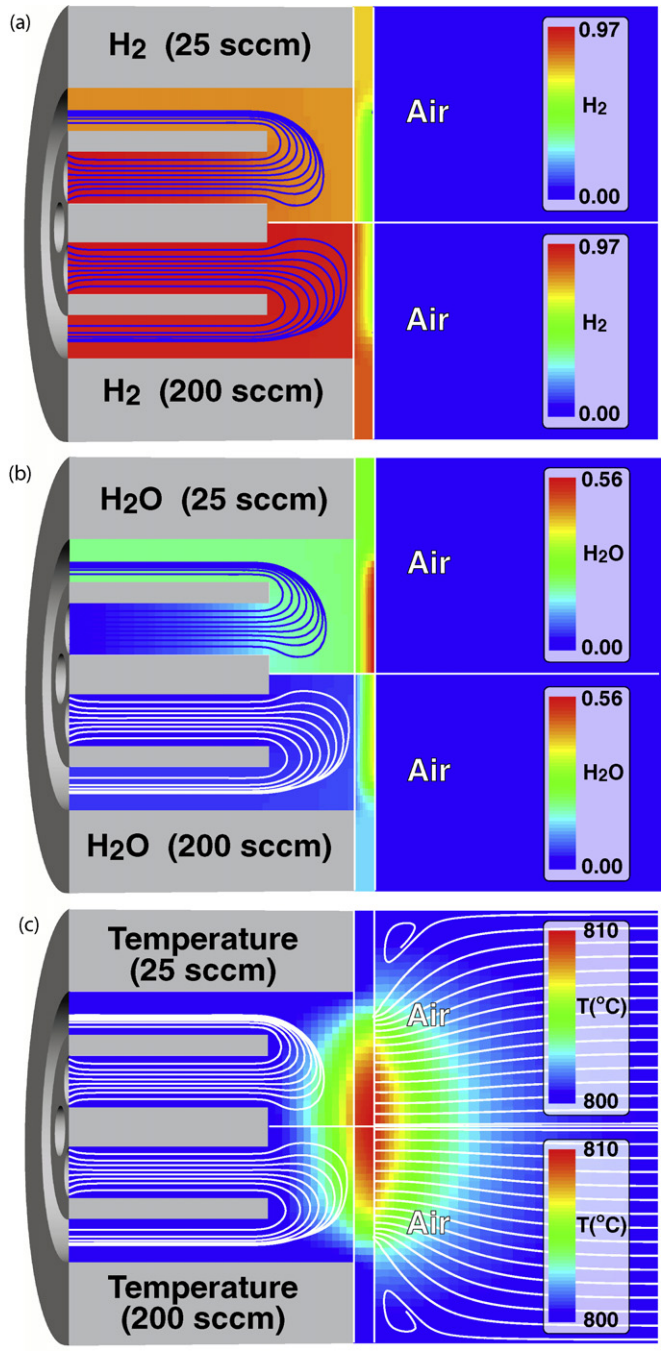

Fig. 6. Contour plots illustrating model solutions for the cell operating with a fuel mixture of 97% H_2, 3% H_2O, operating potential of 0.5 V, and wall temperature of 800 °C. Solutions are shown for fuel flow rates of 25 and 200 sccm. The composition contours are mole fractions. Path lines are superimposed on the contours to show flow patterns.

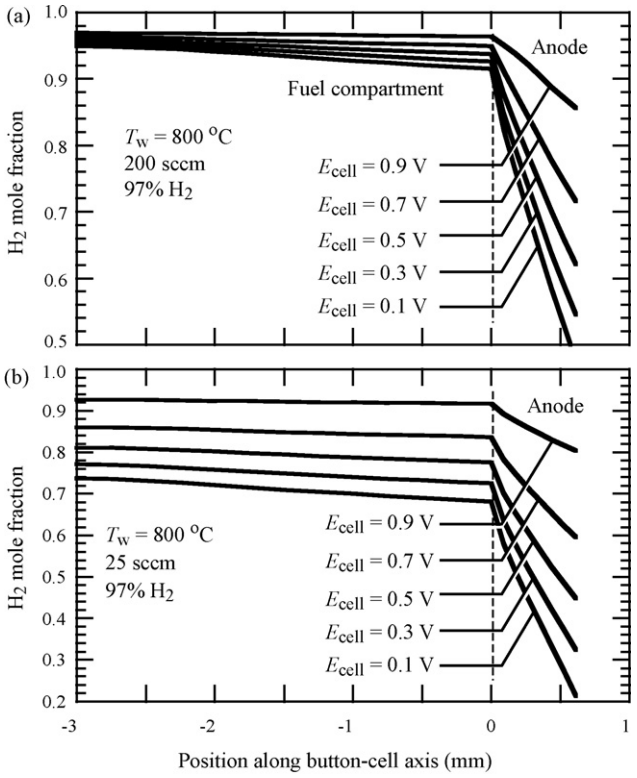

Fig. 7. H_2 mole fraction along the button-cell axis in the fuel chamber and within the anode pore space. Solutions are shown for two fuel flow rates: (a) 200 sccm and (b) 25 sccm.

the interface between the anode gas compartment and the face of the MEA is close to that of the inlet flow. Interpreting experimental results usually depends upon knowing the gas-phase composition within the anode compartment. Thus, it is desirable to maintain sufficiently high flow rates such that there is little fuel depletion and the composition is nearly that of the feed gases.

Fig. 7 shows gas-phase H_2 mole-fraction profiles along the button-cell axis, both in the anode compartment and within the anode pore space. Solutions are shown for flow rates of 200 and 25 sccm. The axial position of $x = 0$ is at the interface between the porous anode and the gas in the anode chamber. The rightmost position at $z = 0.7$ mm is at the anode–electrolyte interface. The cell is operating with humidified hydrogen (i.e., 97% H_2 and 3% H_2O). It is evident that there is considerable hydrogen variation, especially within the porous anode. The variation is greatest at low operating potential, where hydrogen is being consumed at higher rates to support the electrochemical charge transfer. The significantly higher gradients within the anode pore space are due to comparatively high transport resistance in the porous media.

At flow rates of 200 sccm (Fig. 7a), there is relatively little fuel depletion in the anode compartment. The H_2 mole fraction remains greater than 90%, even at the high current densities associated with low operating potential. Under these conditions, the hydrogen profiles are not affected greatly by the isothermal assumption. Although there is no general rule for determining an acceptable level of fuel depletion, maintaining fuel composition within a few percent of the inlet composition is certainly reasonable. As illustrated by Fig. 7 a, inlet flow of 200 sccm in this reactor appears to be sufficiently high even at very low operating potentials. This trend is confirmed by the asymptotic behavior of the experimental polarization curves at high flow rates (Fig. 5).

At a relatively low fuel flow rate of 25 sccm (Fig. 7b), there is significant fuel depletion. Especially at low operating potentials, the H_2 composition in the anode chamber is significantly below the specified inlet composition of 97%. As can also be seen in Fig. 6, at low flow rates there is very significant upstream diffusion well into the feed tube. Quantitative interpretation of button-cell experiments at these low flow rates would depend upon a quantitative understanding of fuel depletion.

In addition to depletion along the centerline axis, there are also radial composition variations. Fig. 8 shows the radially averaged H_2 mole fraction at the interface between the anode and fuel chamber

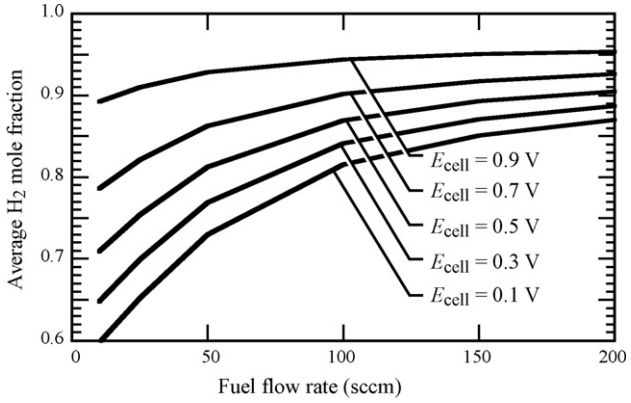

Fig. 8. Average H_2 mole fraction at the interface between the anode and fuel chamber as functions of fuel flow rate and cell potential. In all cases, the inlet fuel is 97% H_2.

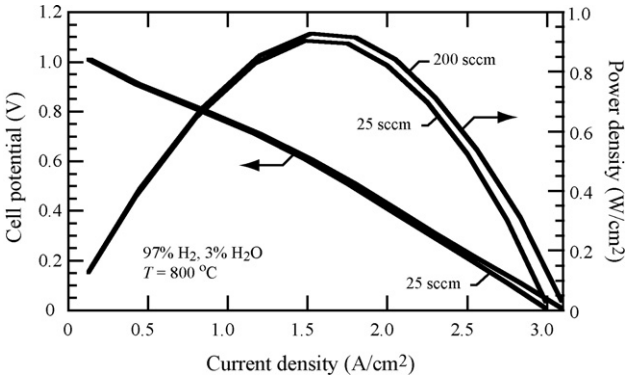

Fig. 10. Predicted polarization characteristics for the button cell operating at 800 °C with a fuel mixture of 97% H_2, 3% H_2O, but with fuel flow rates of either 25 or 200 sccm.

as functions of inlet fuel flow rate at various cell potentials. As current density increases (decreasing cell potential), more fuel is utilized and the H_2 depletion increases. Similarly, as the inlet fuel flow rate decreases, there is less H_2 to mix with the reaction product H_2O, and H_2 dilution increases. For the most extreme case shown in Fig. 8($E_{cell} = 0.1$ V and 10 sccm), the average H_2 mole fraction at the anode interface decreases to around 60%, which is substantially smaller than the inlet mole fraction of 97%.

Fig. 6 c shows that the maximum temperatures within the MEA are some 10 ° C higher than the wall temperatures and the inlet gas temperatures. Fig. 9 shows temperature profiles through the gas compartments and the MEA structure. The highest temperatures are always near dense electrolyte, where the charge-transfer chemistry is active and polarization losses manifest themselves as heat sources. At low operating potential (high current density), the MEA temperatures are nearly 25 ° C higher than the furnace wall temperature. The temperature profiles are found to depend only weakly upon the fuel rates.

It is interesting to note that if radiation from the MEA surface is neglected, the predicted MEA temperatures are significantly greater. Without radiation, the predicted peak MEA temperature is nearly 820 ° C at $E_{cell} = 0.5$ V, and nearly 840 ° C at $E_{cell} = 0.1$ V. It is also interesting to note that the temperature profiles in the gas compartments are nearly linear. Such profiles show that heat transfer through the gas phase is dominated by conduction, not convection. This explains why the temperature profiles depend weakly upon flow fuel rates.

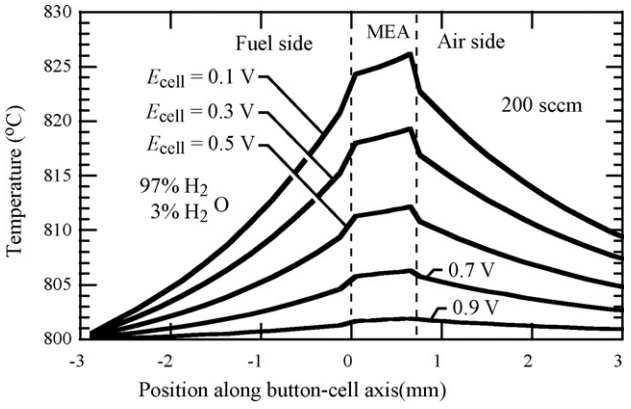

Fig. 9. Centerline temperature profiles through the gas compartments and the MEA structure. In all cases, the cell is operating on an inlet flow rate of 200 sccm of humidified H_2. The wall temperatures and inlet gases are at 800 °C.

It is clear that low flow rates have a significant effect on fuel composition. Interestingly, however, the flow-rate effects on polarization appear to be weak (Fig. 5). Fig. 10 shows model-predicted polarization behavior for 25 and 200 sccm fuel flow rates (corresponding to the calculations shown in Fig. 6). Despite the significant variations in fuel depletion, the predicted effect on polarization is very small. This weak influence is partially due to the functional dependence of the charge-transfer chemistry (i.e., Eq. (20)) and partially due to compensating temperature effects. At low flow rates, the MEA temperatures are slightly higher owing to reduced convective losses. Because of high activation energies, even small temperature variations can be significant.

Although the flow-rate effects on polarization may be weak, it is desirable to establish the minimum flow rates needed to assure that measured results are independent of flow rates. Quantitative interpretation of experimental results depends upon quantitative knowledge of temperature and composition.

7. Performance on CH_4–CO_2

The next set of simulations is based upon a fuel mixture of 75% CH_4 and 25% CO_2 at a relatively low flow rate of 25 sccm (average velocity of 0.16 m s^{-1}). The MEA parameters in Table 1 continue to be used, but detailed reforming chemistry is now included [8]. The fuel mixture is chosen to investigate the effects of internal reforming. In this case, methane reforming proceeds via a combination of two routes. One is dry reforming, using CO_2 as a reforming agent. Second is steam reforming, using electrochemically produced H_2O. Under such operating conditions, carbon deposits are also a consideration. However, the present study does not directly address carbon deposition. Because reforming is an endothermic process, thermal effects within the MEA are more complex than they are with H_2 fuel.

Fig. 11 shows contour plots of species mole fractions and temperature for a nominal operating condition of $E_{cell} = 0.5$ V. With very low Reynolds number Re (order unity), the uniform inlet velocity relaxes quickly within the feed tubes to the laminar Poiseuille parabolic profile.

Fig. 11 a shows contours of CH_4(upper) and H_2 (lower) mole fractions. As the flow approaches the MEA, the CH_4 mole fraction is diluted with CO and H_2O. Because of the relatively low flow rate, there is substantial upstream diffusion. The CH_4 mole fraction at the anode surface is approximately half of the specified inlet value. The lower plot shows significant gas-phase H_2 diffusion upstream into the fuel inlet tube. Because of the low flow velocity and high diffusivity of H_2, there are very significant variations in H_2 throughout the anode compartment.

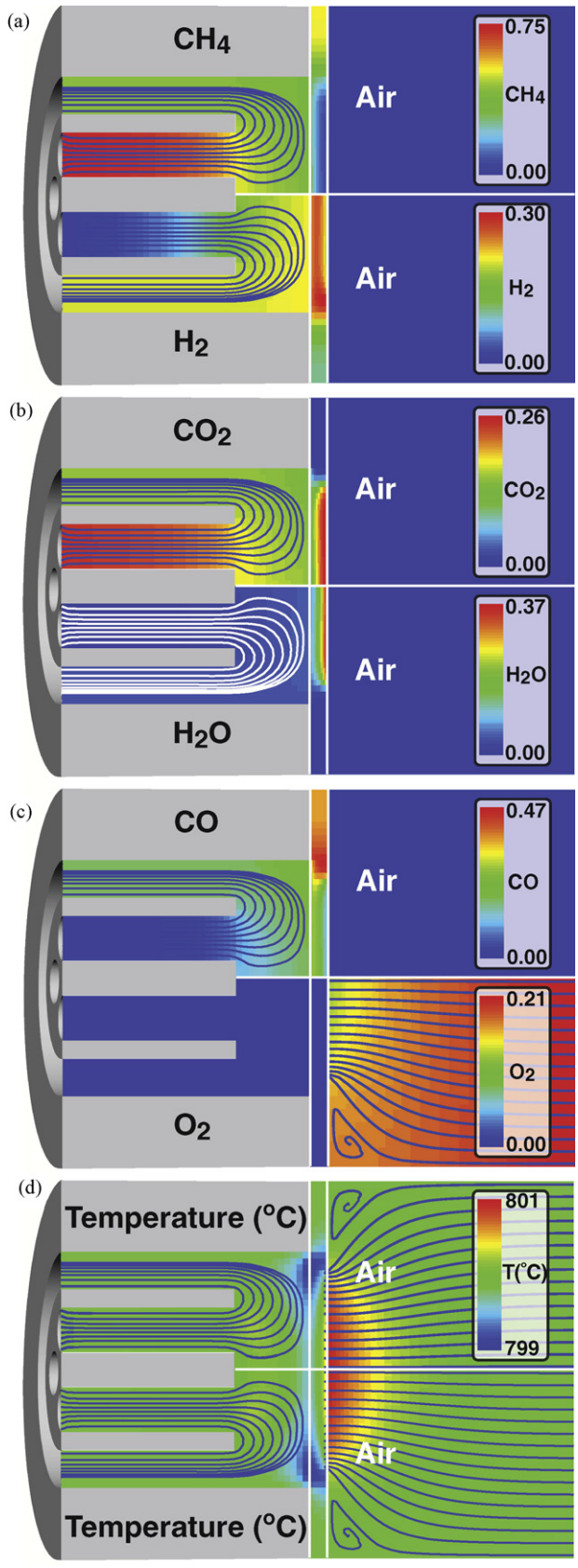

Fig. 11. Contour plots illustrating the solutions for the cell operating with 75% CH_4, 25% CO_2, fuel flow rate of 25 sccm, wall temperature of 800 °C, and $E_{cell} = 0.5$ V. The composition contours are mole fractions. Pathlines are superimposed on the contours to show flow patterns.

Within the porous anode, CH_4 is catalytically reformed on the Ni catalyst surfaces, rapidly producing H_2 and CO. At the interface with the dense electrolyte the CH_4 has been fully converted. The H_2 reaches a peak mole fraction of around 30% in the interior of the anode structure. Near the dense electrolyte, the H_2 is consumed by electrochemical charge-transfer reactions, thus significantly reducing its mole fraction. Relatively high CH_4 mole fractions are seen in the outer radial sections of the MEA. This is a result of the cathode being applied only in the center regions of the disk, eliminating electrochemistry at the outer radial positions. In the outer regions the electrochemistry is inactive and H_2O is not formed, which reduces reforming activity. The CH_4 can diffuse radially outward where it is essentially trapped. In a similar way H_2 can diffuse radially outward within the anode structure. Because H_2 is not being produced by reforming in the outer radial sections, its mole fraction is much lower than in the central regions where reforming is active.

Fig. 11 b shows contours of CO_2(upper) and H_2O (lower) mole fractions. The electrochemically produced H_2O is maximum within the anode near the dense–electrolyte interface. As H_2O is transported toward the anode compartment, it participates in catalytic reforming chemistry to produce H_2. Under the circumstances here, the H_2O is mostly consumed before reaching the anode compartment. Significant levels of CO_2 enter with the fuel. This CO_2 is diluted with CO and H_2 as it flows toward the anode. Within the anode, however, CO_2 is produced catalytically, primarily via water-gas-shift chemistry. That is, H_2O reacts with CO to form H_2 and CO_2. The CO_2 mole fraction is maximum near the dense electrolyte where ample H_2O and CO are present.

Fig. 11 c shows mole fraction contours of CO (upper) and O_2(lower). In regions where charge-transfer chemistry is active, the H_2 is depleted and the water-gas-shift process (globally, $CO + H_2O \leftrightharpoons CO_2 + H_2$) rapidly converts CO to CO_2 and H_2. Thus CO levels remain relatively low in the center regions of the MEA. Interestingly, the CO is maximum within the anode structure near the outer radius of the cathode. In this region, CO is formed primarily by steam reforming. However, because of reduced electrochemical activity beyond the cathode radius, the CO is not converted into CO_2 through the water-gas-shift reaction due to the lower H_2O concentration. CO also diffuses radially outward, where it is essentially trapped. In the outer regions there is little H_2O available, so water-gas shift is relatively inactive.

On the cathode side, air is drawn toward the cathode where it is electrochemically reduced to form oxygen ions in the dense electrolyte. Thus, the O_2 mole fraction is depleted and the relative N_2 fraction increases. In this system there is not a forced air flow. Nevertheless, the path lines show induced flow as air is drawn toward the cathode.

Fig. 11 d is a contour plot of temperatures. At an operating potential of $E_{cell} = 0.5$ V, the thermal consequences of exothermic electrochemical reactions and ohmic heating within the electrolyte are nearly balanced by the endothermic heterogeneous reforming chemistry within the anode. Under these circumstances, the result is nearly isothermal operation, with temperature variations of only a few degrees. Other circumstances, such as illustrated in Fig. 11 d, however, cause larger temperature excursions.

Fig. 12 a illustrates the methane mole fraction as a function of axial position on the button-cell centerline. The position $x = 0$ is at the interface between the porous anode and the fuel gas compartment. At the relatively low fuel flow rate of 25 sccm, it is evident that there is significant fuel depletion, especially at low operating potential. As in the case of H_2 fuel (Fig. 7), the gradients are highest within the porous electrode. This is the result of high transport resistance with the porous media.

Fig. 12 b illustrates H_2mole fraction profiles. Because there is no H_2 in the inlet fuel stream, all the H_2 is produced via catalytic

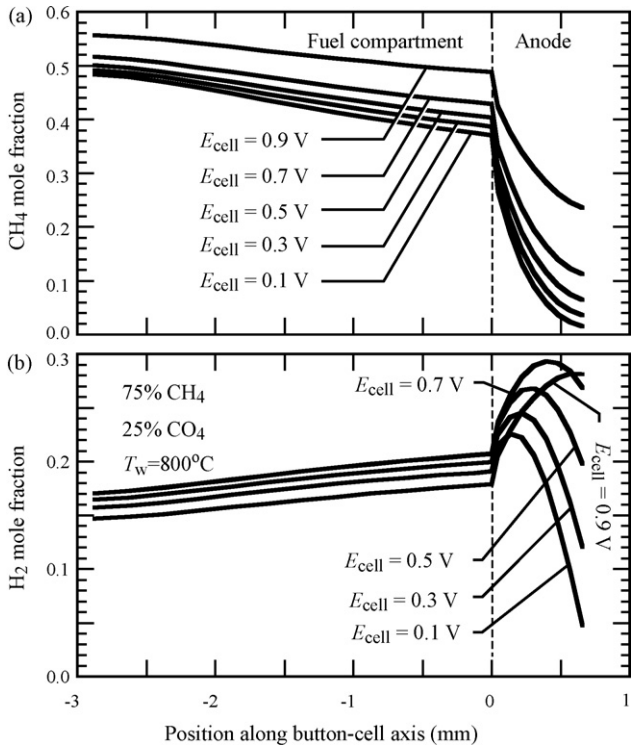

Fig. 12. CH_4 and H_2 mole-fraction profiles along the button-cell axis within the fuel chamber and the anode structure. In all cases, the inlet fuel composition is 75% CH_4 and 25% CO_2 and the wall temperature is 800 °C.

reforming processes within the anode. The H_2 mole fraction is maximum within the anode. It is transported toward the dense electrolyte interface where it is consumed via charge-transfer reactions. Hydrogen is also transported into the anode gas compartment. At the low flow rate here (25 sccm), the H_2 transport from the anode structure is sufficient to maintain significant levels of H_2 within the anode gas compartment. It is also interesting to note that at high operating potentials (low current) relatively little of the catalytically formed H_2 is consumed electrochemically. In this case, the H_2 is formed primarily by dry reforming, and the peak mole fraction is near the dense electrolyte interface.

Fig. 13 shows radial profiles of methane mole fraction at the interface between the anode and the fuel chamber. Significant radial variations are evident. It is interesting to note that the CH_4 mole fraction increases toward the outer edges of the anode. Recall

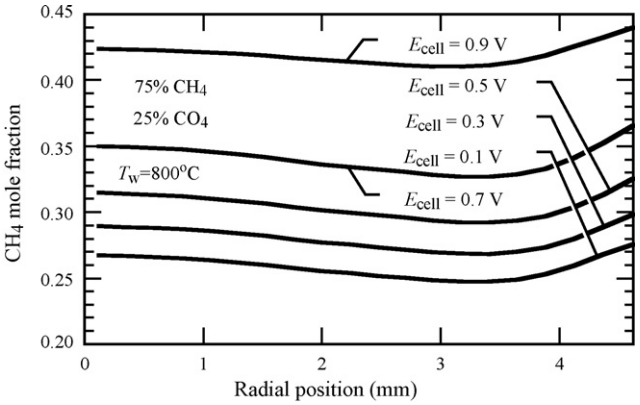

Fig. 13. Radial profiles of CH_4 mole fraction on the anode top surface. In all cases, the inlet fuel composition is 75% CH_4 and 25% CO_2. The wall temperature is 800 °C.

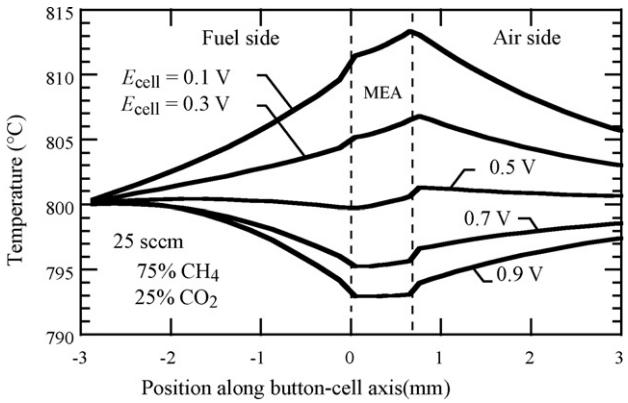

Fig. 14. Temperature profiles along the button-cell axis. The inlet fuel is a mixture of 75% CH_4 and 25% CO_2 at a flow rate of 25 sccm.

that in this cell, the outer radius of the cathode layer is only 4 mm. Thus, beyond a radius of 4 mm, there is no electrochemical steam production, which reduces the steam-reforming rate. Also, some of the hydrogen and CO produced via reforming can diffuse radially into the outer regions of the porous anode. Because in this region the H_2 is not consumed electrochemically, surface chemistry can regenerate the CH_4. The simulations here suggest that a higher fuel flow rate is desirable. Increasing the flow rate will reduce radial variations and bring the fuel composition at the anode face closer to the inlet composition.

Fig. 14 shows axial temperature profiles along the button-cell axis. In all cases the fuel is a mixture of 75% CH_4 and 25% CO_2 at 25 sccm and the furnace walls are fixed at 800 °C. At high current (low cell potential) the MEA temperature exceeds the gas temperatures on both the fuel and air sides. This is because the ohmic heating and charge-transfer exotherms exceed the endothermic effects of on-anode reforming. At low current, however, the situation is opposite. Under these conditions the reforming endotherm dominates and the MEA temperature is below the temperatures in the gas compartments.

8. Flow rates and cell performance

Understanding fuel-depletion effects is an important aspect of understanding SOFC performance. Operating with high flow rates is not in conflict with investigating fuel-depletion effects. As is done in button-cell experiments by Jiang and Virkar [12], the fuel compositions can be deliberately premixed to simulate various depletion environments that occur in full stacks and systems. However, each button-cell experiment is run under flooded conditions such that there is no ambiguity about the gas-compartment composition.

All other things being equal, fuel flow rates should be sufficiently high that fuel depletion is negligible and the gas-phase composition in the anode compartment is essentially that of the feed gas. In principle this approach simplifies analysis and interpretation of experimental data. However, when using hydrocarbon fuels and Ni-based anodes, carbon deposits are potentially problematic. As fuel flow rates are reduced, the hydrocarbon fuel is diluted with steam and CO_2, and hence the propensity for carbon deposition on Ni surfaces is reduced.

Although using low fuel flow rates may complicate analysis, preventing carbon deposits is essential. A cell that fails to operate due to carbon fouling is of very little value. With low fuel flow rates and high depletion and dilution, it should be recognized that the composition of the fuel seen by the MEA can be significantly different from the inlet feed composition. To be quantitatively useful,

models that are used to interpret the data must accommodate the gas-phase composition variations within the anode compartment.

Fig. 11 shows that with low fuel flow rates the CH_4 is very significantly diluted with H_2O and CO_2 at the face of the anode, which contains Ni. Such dilution of the hydrocarbon enables deposit-free operation, even in the presence of Ni. However, it may also be noted that there are alternatives for deposit-free operation. One possibility is to use electrode materials, such as doped perovskites, that do not promote coke formation [18]. In this case, high fuel flow rate and lower depletion is practical.

9. Natural convection and axisymmetry

With local temperature variations and a horizontal orientation of the cell, it is reasonable to anticipate that natural convection might play a role and induce three-dimensional flow fields. However, for the conditions studied here, the results show that natural convection plays a negligible role.

The potential influence of natural convection behavior can be understood in the context of a dimensionless groups. Buoyant effects are typically negligible when

$$\frac{\mathrm{Gr}}{\mathrm{Re}^2} < 1, \tag{25}$$

where the Grashof and Reynolds numbers are defined as

$$\mathrm{Gr} = \frac{g\beta\Delta T L^3}{\nu^2}, \quad \mathrm{Re} = \frac{UL}{\nu}. \tag{26}$$

In these definitions g is the gravitational constant, β is the volumetric thermal-expansion coefficient, ΔT is a characteristic temperature difference, U is a characteristic velocity, L is a characteristic length scale, and ν is the kinematic viscosity. For this cell configuration the characteristic length scale for the Reynolds number is the distance between the inlet tube and the anode face (here 3 mm) and the characteristic velocity is the mean inlet velocity. Because of the horizontal orientation, the characteristic length scale for the Grashof number is the MEA diameter. Assuming a characteristic temperature difference on the order of 10 °C, $\mathrm{GrRe}^2 \approx 1$. Thus, the fact that the three-dimensional simulations deliver essentially axisymmetric results is entirely reasonable.

As an example that illustrates one aspect of the axisymmetry, consider surface coverages within the porous anode structure. Fig. 15 shows contours of the CO(s) coverage in a plane through the middle of the anode ($E_{\mathrm{cell}} = 0.5$ V). The axisymmetry is evident from the bulls-eye shape of the contours. Similar results are found for all fluid variables at all flow rates, temperatures and operating potentials.

An axisymmetric model for this button cell would be quite accurate (i.e., three-dimensional effects are found to be negligible). Of course, larger dimensions, lower flow rates, or higher temperatures, can lead to circumstances in which buoyant effects could become important.

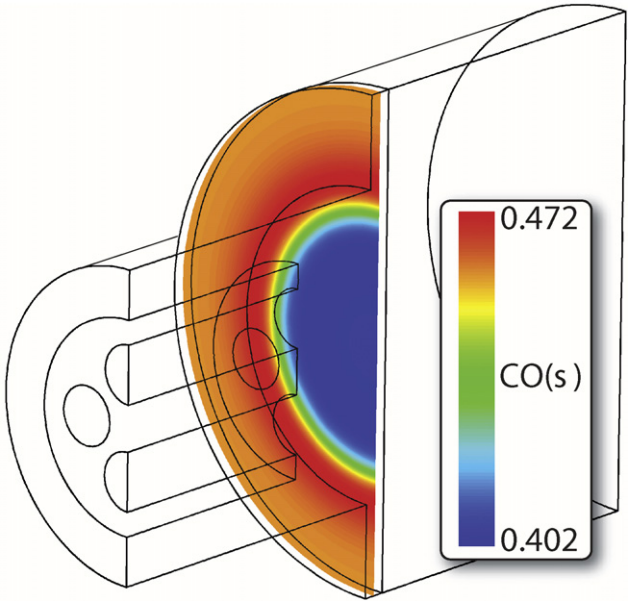

Fig. 15. CO(s) surface fractional coverage in the mid-anode plane. The cell is operating with a fuel flow rate of 25 sccm, nominal temperature of 800 °C, and $E_{\mathrm{cell}} = 0.5$ V. The coverage ranges from low in the center regions (blue contours) to high at the outer radii (red contours). (For interpretation of the references to colour in this figure legend, the reader is referred to the web version of the article.)

10. Summary and conclusions

Button-cell experiments are used widely in the development of new SOFC materials and MEA architectures. Data usually consist of polarization characteristics and sometimes electrochemical impedance spectra. The experimental conditions are usually represented in terms of inlet fuel composition and flow rate, cell temperature, and operating potential.

In analyzing and interpreting button-cell experiments, two important assumptions are typically applied. First, it is assumed that the flow rates are sufficiently high that the species composition at the interface between the gas compartment and the anode structure is the same as inlet fuel mixture. In other words, the fuel is minimally depleted and diluted. Second, the gases and the MEA are assumed to be isothermal. If either of these assumptions is not valid, then the data interpretation can be flawed.

In this paper a new three-dimensional computational fluid dynamics model is used to characterize physical and chemical behavior in SOFC button cells. The primary purpose is to investigate how the assumptions noted above depend upon cell operating conditions. The model includes coupled fluid flow, heat transfer, and multi-component species transport. It also includes porous-media transport, elementary catalytic chemistry within electrode structures, and electrochemical charge transfer.

The model is implemented in object-orientated C++. It uses geometrically flexible unstructured grids, which incorporate fluid regions and solid materials. The open-source Cantera software is used to evaluate thermodynamic and transport properties, as well as reaction chemistry.

Although the model can be applied to general geometries, it is used here to simulate a particular button cell that has been experimentally measured. Results show that if inlet flow rates are too low, there can be significant compositional variations in the gas compartments. When this is the case, it is not appropriate to analyze data using the assumption that the MEA is exposed to the fuel composition that is supplied through the feed lines. However, it is possible to increase flow rates to the point that gas composition is minimally depleted and diluted. Models, such as the one in this paper, provide the quantitative means to establish the appropriate operating conditions.

Because the button-cell in this study is oriented horizontally, there is the possibility for buoyant convection to cause three-dimensional flow patterns. Such behavior could further complicate data interpretation. However, because of relatively small dimensions and temperature variations, the results show that buoyant convection is easily overcome. Thus, even under circumstances with low flow rates high fuel depletion, assuming axisymmetric flow is valid.

Acknowledgements

This work at the Colorado School of Mines and Ansys/Fluent was supported by the Office of Naval Research through a Research Tools Consortium grant number N00014-05-1-0339. The effort at Northwestern University was supported by the Department of Energy National Energy Technology Laboratory under Award Number DE-FC26-05NT42625. We gratefully acknowledge the collaboration with Prof. David Goodwin (Caltech) for his assistance in integrating CANTERA into these simulations.

References

[1] Z. Zhan, Y. Lin, M. Pillai, I. Kim, S.A. Barnett, J. Power Sources 161 (2006) 460–465.
[2] Y. Shi, N. Cai, C. Li, J. Power Sources 164 (2007) 639–648.
[3] V.M. Janardhanan, O. Deutschmann, J. Power Sources 162 (2006) 1192–1202.
[4] R. Suwanwarangkul, E. Croiset, E. Entchev, S. Charojrochkul, M.D. Pritzker, M.W. Fowler, P.L. Douglas, S. Chewathanakup, H. Mahaudom, J. Power Sources 161 (2006) 308–322.
[5] Y. Shi, N. Cai, C. Lia, C. Bao, E. Croiset, J. Qian, Q. Hu, S. Wang, J. Power Sources 172 (2007) 235–245.
[6] Y. Shi, N. Cai, C. Lia, C. Bao, E. Croiset, J. Qian, Q. Hu, S. Wang, J. Power Sources 172 (2007) 246–252.
[7] D.S. Monder, K. Nandakumar, K.T. Chuang, J. Power Sources 162 (2006) 400–414.
[8] H. Zhu, R.J. Kee, V.M. Janardhanan, O. Deutschmann, D.G. Goodwin, J. Electrochem. Soc. 152 (2005) A2427–A2440.
[9] H. Zhu, R.J. Kee, J. Electrochem. Soc. 155 (2008) B715–B729.
[10] R.J. Kee, M.E. Coltrin, P. Glarborg, Chemically Reacting Flow: Theory and Practice, John Wiley, New York, 2003.
[11] H. Zhu, R.J. Kee, ECS Trans. 7 (2007) 1869–1878.
[12] Y. Jiang, A.V. Virkar, J. Electrochem. Soc. 150 (2003) A942–A951.
[13] A.M. Sukeshini, B. Habibzadeh, B.P. Becker, C.A. Stoltz, B.W. Eichhorn, G.S. Jackson, J. Electrochem. Soc. 153 (2006) A705–A715.
[14] S. Mathur, J. Murthy, Numer. Heat Transf. 31 (1997) 195–215.
[15] S.V. Patankar, Numerical Heat Transfer and Fluid Flow, McGraw-Hill, New York, 1980.
[16] K. Stueben, in: C.W. Oosterlee, U. Trottenberg, A. Schuller (Eds.), Multigrid, Academic Press, New York, 2001, pp. 413–532.
[17] D.G. Goodwin, in: M. Allendorf, F. Maury, F. Teyssandier (Eds), Chemical Vapor Deposition XVI and EUROCVD 14, vol. PV 2003–08, pp. 155–162. Electrochemical Society, 2003 (see also http://www.cantera.org).
[18] M.R. Pillai, Y. Jiang, N. Mansourian, I. Kim, D.M. Bierschenk, H. Zhu, R.J. Kee, S.A. Barnett, Electrochem. Solid-State Lett. 11 (2008) B174–B177.